Oxygen defects: The key parameter controlling the activity and selectivity of mesoporous copper-doped ceria for the total oxidation of naphthalene

Asunción Aranda [a], Said Agouram [b], Jose M. López [a], Ana M. Mastral [a], David R. Sellick [c], Benjamín Solsona [d],[*], Stuart H. Taylor [c],[**], Tomás García [a],[***]

[a] *Instituto de Carboquímica (CSIC), C/Miguel Luesma, 50018 Zaragoza, Spain*
[b] *Department of Applied Physics, Universitat de València, Burjassot, Valencia, Spain*
[c] *Cardiff Catalysis Institute, School of Chemistry, Cardiff University, Main Building, Park Place, Cardiff CF10 3AT, UK*
[d] *Departament d'Enginyeria Química, Universitat de València, C/Dr. Moliner 50, 46100 Burjassot, Valencia, Spain*

ABSTRACT

Mesoporous CeO$_2$ modified by the addition of copper has shown high efficiency for the total oxidation of naphthalene. High activity and 100% selectivity to carbon dioxide throughout the whole range of temperatures studied were achieved for copper loadings of 3.6% and lower. The catalytic behaviour has been related to the concentration of surface oxygen defects. A clear correlation between the concentration of surface oxygen defects (determined by XPS and DRIFTS) and the catalytic performance has been identified. Catalytic activity increased as copper was incorporated into the ceria up to 3.6%. In this range of copper content the copper was incorporated into the cubic fluorite lattice of CeO$_2$ and this was confirmed using XRD and electron diffraction studies. For copper ceria catalysts with higher copper contents the concentration of oxygen defects decreased and an additional dispersed monoclinic CuO phase with a low intrinsic activity was formed, thus leading to a decrease of both the activity and the selectivity to CO$_2$.

© 2012 Elsevier B.V. All rights reserved.

1. Introduction

Currently, increasingly strict environmental legislation and more demanding production efficiency and quality standards means that catalysis is essential in many existing and emerging processes. Within the vast number of applications of catalysis, those with environmental protection purposes have experienced a major increase in recent years. Amongst these, the elimination of atmospheric contaminants – such as NO$_x$ removal [1,2] and Volatile Organic Compound (VOC) abatement – has generated major interest with respect to their effects on human health and environmental impact [3]. Improved catalysts for the complete oxidation of VOCs are being approached in different ways. One approach is developing catalysts of innovative composition, e.g. the use of supported noble metal catalysts [4–6], combinations of noble/non-noble metal oxides [7–9], and different metal oxide compositions [10]. The other approach has focussed efforts towards materials design, aiming to control the final properties of the catalysts from the synthesis stage [11–16].

An important family of VOCs is the Polycyclic Aromatic Hydrocarbons (PAHs), generated in the incomplete combustion or pyrolysis of carbonaceous materials, e.g. in internal combustion engines [17], power generation stations [18] and many industrial plants [19–21]. Due to their toxic, carcinogenic, bio accumulative and/or mutagenic nature, even at low concentrations [22–24], since 1998 PAHs are listed as Persistent Organic Pollutants which must be eliminated [25]. PAHs are released in flue gases, both supported on particulate matter and/or in the gas phase, in the parts per million concentration range [26]. Whereas supported PAHs can be trapped with particulate matter abatement devices [27], their elimination in the gas phase requires the treatment of high volume low concentration gas streams. The technologies considered to reduce gaseous PAH emissions include biodegradation [28], adsorption [29], absorption [30], high-energy electron beam treatment [31], thermal oxidation [25] and catalytic oxidation, which has been demonstrated to be one of the most promising options due to its high efficiency and a lower energy penalty [3–5,32,33].

Within the classification of PAHs, naphthalene is usually considered as a suitable model compound, since it is one of the most abundant PAHs in flue gases, the simplest and least toxic, and representative in studies of PAH elimination [6,34,35]. Several studies have explored the use of noble metal catalysts for naphthalene

* Corresponding author. Tel.: +34 963544319.
** Corresponding author. Tel.: +44 29 208 74062.
*** Corresponding author. Tel.: +34 976 733977; fax: +34 976 733318.
E-mail addresses: benjamin.solsona@uv.es (B. Solsona), taylorsh@cardiff.ac.uk (S.H. Taylor), tomas@icb.csic.es (T. García).

Table 1
Physicochemical properties and specific catalytic activity of copper ceria catalysts.

Catalyst	Cu/(Ce + Cu) at. ratio[a]	S_{BET}[b] ($m^2\,g^{-1}$)	V_{BJH}[c] ($cm^3\,g^{-1}$)	Areal rate$_{CO_2}$[d] ($g_{CO_2}\,m^{-2}\,h^{-1}$)	Selectivity[e] (%)
CeO_2	0	43	0.11	0.25	70
$Ce_{0.993}Cu_{0.007}O_2$	0.007	40	0.11	1.77	>99
$Ce_{0.988}Cu_{0.012}O_2$	0.012	49	0.13	4.63	>99
$Ce_{0.984}Cu_{0.016}O_2$	0.016	51	0.15	5.06	>99
$Ce_{0.975}Cu_{0.025}O_2$	0.025	50	0.13	3.57	>99
$Ce_{0.964}Cu_{0.036}O_2$	0.036	69	0.19	2.80	>99
$Ce_{0.86}Cu_{014}O_2$	0.14	70	0.21	0.29	46
CuO	1	63	n.d.	0.12	31

[a] Determined by EDX.
[b] Surface area deduced from the isotherm analysis in the relative pressure range 0.05–0.25.
[c] Mesopore volume calculated from the desorption branch of the isotherm using the BJH method.
[d] Formation rate of CO_2 normalized for surface area at 200 °C.
[e] Selectivity to CO_2 at 20% naphthalene conversion.

abatement, e.g. Pt, Pd and Au [4–6], and these generally show high conversion. Nevertheless, current research efforts are mainly focussed on the development of more active and cost-effective catalysts for the complete oxidation of PAHs, like non-noble metal oxides [16]. Thus, for these materials, the improvement of the synthesis methods can provide better control of the catalyst properties, increase the total efficiency and also help to widen our knowledge about structure–activity relationships [13,15,16]. In previous studies, we have explored the influence of the catalyst porosity on naphthalene total oxidation, studying mesoporous cerium oxide obtained by nanocasting [12,15,16]. The results indicate that a highly ordered structure does not necessarily improve the activity for this reaction. In fact, the most effective catalysts were those with less ordered structures, but with the highest number of oxygen defects and reducibility.

Copper oxide is a versatile catalyst and is active for a range of reactions [36–39] and has shown promising results for the total oxidation of a range of VOCs [2] including naphthalene total oxidation [36]. Additionally, published results show that doping CeO_2 catalysts with copper improves the oxygen storage capacity, diffusivity and redox properties, which are attributed to the formation of structural defects [40]. $CuO–CeO_2$ composite catalysts have been demonstrated to be very promising for CO oxidation [41] and benzene oxidation [42], and hence could be a potential candidate as a catalyst for naphthalene total oxidation. However, this hypothesis needs to be explored as efficient catalysts for either the oxidation of CO or benzene have been shown to follow different trends when tested for the oxidation of naphthalene [34]. Initial studies showed very promising naphthalene total oxidation activity for the copper modified mesoporous CeO_2 catalyst [43], and the present study presents a more detailed investigation. A range of different non-ordered $CuO–CeO_2$ mesoporous composites have been synthesized and tested. Moreover, thorough catalyst characterisation was carried out to gain a better understanding of the key parameters controlling the improved performance of copper doped CeO_2 catalysts for naphthalene catalytic combustion.

2. Experimental

2.1. Preparation of mesoporous cerium oxides

For the synthesis of the mesoporous cerium oxide, a synthesis method previously published by Hu *et al.* [42] was used. In a typical experiment, appropriate molar quantities of $Cu(NO_3)_2 \cdot 3H_2O$, and $Ce(NO_3)_3 \cdot 6H_2O$, along with 30.0 g NH_4NO_3, and 0.5 wt% polyethylene glycol (PEG) were dissolved in 100 mL of deionized water to form a solution with a metal ion concentration of 0.1 M 15% aqueous ammonia, together with 0.5 wt% NH_4PPA (ammonium polyacrylate), were added to the above solution until the solution pH was

9. The precipitate was aged for 10 min, followed by filtration and drying at 50 °C for 12 h. The resulting powders were calcined at 600 °C for 4 h to form the mesoporous structured catalysts. By this method, 6 different catalysts were prepared, varying the Cu/Ce ratio and they were labelled $Ce_{1-x}Cu_xO_2$, where x is the nominal relative molar concentration of Cu in the catalyst (Table 1). For comparative purposes, a mesoporous CeO_2 powder was prepared using the same conditions, but without copper addition. Finally, a pure CuO catalyst was also prepared by a precipitation method. In this case, an aqueous solution (0.25 M) of the copper nitrate salt was stirred at 80 °C and aqueous sodium carbonate (0.25 M) was added dropwise until a pH of 9 was obtained. The resulting solution was stirred and aged for 1 h at 80 °C. The precipitate was collected by filtration and after drying in an oven at 120 °C the catalyst was calcined in static air at 600 °C for 2 h.

2.2. Catalyst characterisation

Catalyst samples were characterised by N_2 adsorption at −196 °C, using a Micromeritics ASAP 2020 apparatus. Samples were degassed at 150 °C prior to analysis. From these data, the following textural parameters were calculated: total pore volumes were calculated using the adsorbed volume at a relative pressure of 0.97. Multipoint Brunauer–Emmet–Teller (BET) surface area (S_{BET}) was estimated from the relative pressure range from 0.05 to 0.25. The pore size distribution of the mesoporous materials was analysed using the Barrett–Joyner–Halenda (BJH) method.

Powder X-ray diffraction (XRD) was used to identify the crystalline phases present in the catalysts. A Bruker D8 Advance diffractometer with monochromatic Cu Kα source operated at 40 kV and 40 mA was used. The experimental patterns were calibrated against a silicon standard and the crystalline phases were identified by matching the experimental patterns to the JCPDS powder diffraction file database.

Raman spectra were obtained using a Renishaw system-1000 dispersive laser Raman microscope. The excitation source used was an argon ion laser (514.5 nm) operated at a power of 20 mW. The laser was focused on powdered samples placed on a microscope slide to produce a spot size ca. 3 μm in diameter. A backscattering geometry with an angle of 180° between illuminating and collected radiation was used for recording data.

Temperature programmed reduction (TPR) studies were performed using a Micromeritics Autochem II instrument with a thermal conductivity detector. In all the experiments, 10%vol. H_2 in Ar, at a constant flow rate of 50 ml min^{-1}, was used as reducing gas. A temperature range of 30–800 °C and a constant heating rate of 10 °C min^{-1} were used. In each experiment, 0.30 g of powdered catalyst was analysed.

X-ray photoelectron spectroscopy (XPS) measurements were made on an Omicron ESCA+ photoelectron spectrometer using a non-monochromatized Mg Kα X-ray source ($h\nu = 1253.6$ eV). An analyser pass energy of 50 eV was used for survey scans and 20 eV for detailed scans. Binding energies are referenced to the C1s peak from adventitious carbonaceous contamination, assumed to have a binding energy of 284.5 eV. XPS data were analysed using CasaXPS software. Shirley background subtraction was applied to all the raw data. All the peaks of the corrected spectra were fitted with a Gaussian–Lorentzian shape function to peak fit the data. Iterations were performed using the Marquardt method. Standard deviations were always lower than 1.5%.

Further characterisation of the samples was performed by Transmission Electron Microscopy (TEM), high resolution TEM (HRTEM) and Energy Dispersive X-ray Spectroscopy (EDX) by using a Field Emission Gun (FEG) TECNAI G2 F20 microscope operated at 200 kV. In order to prepare the TEM samples, the Ce–Cu–O powder samples were treated by sonicating in absolute ethanol for several minutes, and a drop of the resulting suspension was deposited onto a holey-carbon film supported on a nickel grid, which was subsequently dried. The samples were also used to determine the elemental composition and distribution of cerium and copper by using EDX-mapping.

Diffuse Reflectance Fourier Transform Infrared spectroscopy (DRIFTS) studies were carried out with a VERTEX 70 FTIR instrument operated with OPUS software. A spectratech DRIFTS high-temperature cell was filled with the powdered sample. The required gas flow (synthetic air or naphthalene in N_2) of 25 ml min^{-1} was maintained by mass-flow controllers. Moisture free catalyst spectra were obtained after heating the sample at 150 °C for 30 min. Prior to the in situ adsorption/reaction measurements by DRIFTS at 250 °C, the samples were activated at 400 °C for 30 min in synthetic air flow. Each spectrum presents an average of 32 scans collected with a spectral resolution of 2 cm^{-1}. The spectra shown were obtained after subtraction of the features of the catalyst, recorded at 250 °C in He. Below 750 cm^{-1} the spectra showed specular reflections and, therefore, this region is not included in the discussion.

2.3. Catalyst performance

Catalytic activity tests for naphthalene oxidation were carried out in a fixed bed laboratory micro-reactor. Blank tests were conducted by passing naphthalene (450 ppmv) through an empty reactor that was heated from 100 °C to 350 °C at a rate of 10 °C min^{-1}. Catalysts (pelletized to 0.1–0.2 mm particle size) were tested using a 3/8″ o.d. quartz tube as the reactor. The reaction feed consisted in all cases of ca. 450 ppmv naphthalene in a mixture of 20 vol.% oxygen and 80 vol.% helium. A total flow rate of 50 ml min^{-1} was used and the catalysts occupied a constant volume, giving a GHSV of ca. 75,000 h^{-1} for all the catalysts. Analyses were performed by an on-line gas chromatograph with thermal conductivity and flame ionization detectors. The catalytic activity was measured over the temperature range of 100–350 °C, in incremental steps of 25 °C and temperatures were controlled by a thermocouple, placed in the catalyst bed. Data were obtained at each temperature after naphthalene adsorption equilibrium was accomplished and steady state activity attained. Four consistent analyses were made at each temperature and average values were calculated. The reaction temperature was increased and the same procedure followed to determine each data point. Oxidation activity was expressed as yield of carbon dioxide. Apart from CO_2 other by-products, such as phenanthrene, naphthalene dione, dimethyl phthalate, benzene, alkyl benzenes, benzaldehyde, toluene and xylenes were identified for some of the catalysts tested.
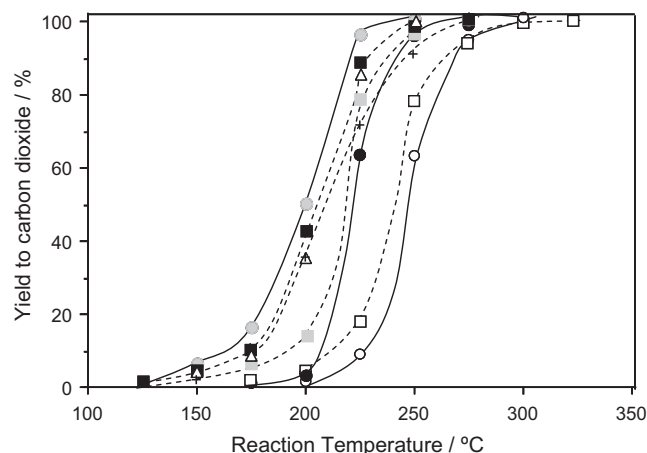

Fig. 1. Variation of the catalytic activity for naphthalene oxidation (expressed as yield to CO_2) as a function of reaction temperature for CeO_2–CuO catalysts. Reaction conditions in text. Catalysts: CeO_2 (●); $Ce_{0.993}Cu_{0.007}$ (▨); $Ce_{0.988}Cu_{0.012}$ (■); $Ce_{0.984}Cu_{0.016}$ (◉); $Ce_{0.975}Cu_{0.025}$ (△); $Ce_{0.964}Cu_{0.036}$ (+); $Ce_{0.86}Cu_{0.14}$ (□), CuO (○).

3. Results and discussion

3.1. Catalyst performance

In order to ascertain contributions from heterogeneously catalysed reactions and those from homogeneous gas phase reactions, naphthalene oxidation was evaluated in an empty reactor. Naphthalene oxidation in the empty reactor was negligible below 350 °C, where a low conversion of ca. 1% was obtained, suggesting that any oxidation activity below 350 °C can be attributed entirely to the presence of the catalysts.

Fig. 1 shows the variation of the catalytic activity, expressed as conversion to CO_2, for naphthalene total oxidation, as a function of the reaction temperature for the range of copper ceria catalysts. For comparative purposes, the activity of the mesoporous CeO_2, prepared by the same method, and CuO prepared by a similar procedure are also included. Excellent catalytic performance was observed for the mixed Ce–Cu–O composite catalysts. They all showed higher catalytic activity than the reference CeO_2 catalyst, with the exception of the Ce–Cu–O catalyst with the highest (14 at.%) copper content, as it had lower catalytic activity than the CeO_2 reference catalyst across the full range of conversion. Fig. 2 presents the values for T_{10} and T_{50}, which are the temperatures
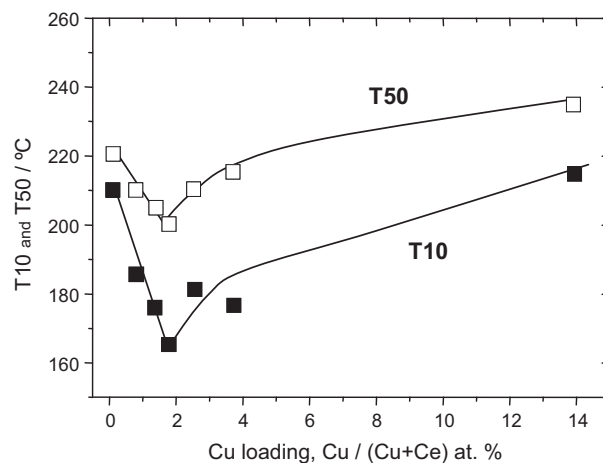

Fig. 2. Influence of the copper loading on the T_{10} (■) and T_{50} (□) values for CeO_2–CuO catalysts. *Note*: T_{10} and T_{50} are the reaction temperatures required for 10 and 50% naphthalene conversion to CO_2, respectively.

required for 10 and 50% yields of CO_2, and the data emphasizes the enhanced catalytic performance of copper ceria catalysts with low copper content. Due to the fact that activity generally decreased with increasing copper content, a catalyst with a much higher (14%) copper content was also studied for interest. The activities of the catalyst synthesized in the present work decrease in the following order:
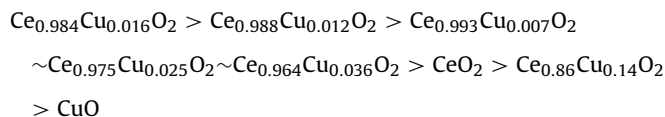
$$Ce_{0.984}Cu_{0.016}O_2 > Ce_{0.988}Cu_{0.012}O_2 > Ce_{0.993}Cu_{0.007}O_2$$

$$\sim Ce_{0.975}Cu_{0.025}O_2 \sim Ce_{0.964}Cu_{0.036}O_2 > CeO_2 > Ce_{0.86}Cu_{0.14}O_2$$

$$> CuO$$

Table 1 shows the selectivity to CO_2 at 20% naphthalene conversion. For the CeO_2 reference catalyst, although the main reaction product observed for naphthalene oxidation was CO_2, this was not the only product. Other compounds such as naphthenol, dimethyl phthalate, benzaldehyde and trace quantities of some others were detected. Conversely, all the Ce–Cu–O catalysts, except the one with the highest copper loading, showed selectivity over 99% towards CO_2 over the entire range of naphthalene conversion. This behaviour is very important for applications in environmental protection, since the formation of byproducts, which can be more toxic than the original pollutants, are avoided.

It is also noteworthy that several cycles of catalytic activity were conducted over the best Ce–Cu–O catalyst ($Ce_{0.984}Cu_{0.016}O_2$). On reuse no remarkable difference of activity or selectivity was observed when compared to data for the fresh catalyst after five cycles. In addition, this catalyst showed stable naphthalene conversion for more than 70 h at 200 °C, which was selected as conversion was less than 100% and so potential deactivation would be readily observed. Furthermore, the same catalyst also showed stable 100% conversion when tested at higher temperature for 70 h.

3.2. Catalyst characterisation

The presence of mesoporosity was assessed from the N_2 physisorption isotherms of the copper ceria catalysts (Fig. 3A). It can be observed that the isotherms show similar profiles in all cases, exhibiting a marginal increase in slope at a relative pressure of ca. 0.5, followed by a linear increase up to 0.8–0.9 in both the adsorption and the desorption branches. The increase in slope at ca. 0.5 corresponds to capillary condensation, typical of mesoporous materials, whilst the further increase at higher relative pressures indicates the presence of macroporosity, which appears to be more substantial at higher copper content. The presence of macroporosity could be due to void space within the samples in addition to being a structural feature. The capillary condensation step is not particularly pronounced; the isotherm shape is an intermediate between type II and type IV. The presence of a broad pore size distribution is confirmed by the occurrence of a rather broad BJH pore diameter distribution [44] in the mesopore size region, together with the formation of some macropores at higher copper content. In addition, it can be observed in Fig. 3B that both the amount of mesopores and the width of the mesopore size distribution increase with the increasing copper content and overall the pore size distribution is shifted to larger values. The specific surface areas of mesoporous CeO_2, estimated from the BET method (Table 1), increase with the increasing copper content. The lowest value of $40 \, m^2 \, g^{-1}$ for the catalyst with the lowest copper content was comparable to the pure CeO_2 ($43 \, m^2 \, g^{-1}$). The successive addition of copper proportionally increased the catalysts surface areas up to $70 \, m^2 \, g^{-1}$ for the material containing 14% copper.

Fig. 4 shows the wide-angle XRD patterns of the mesoporous copper ceria catalysts synthesized in the present work. It was
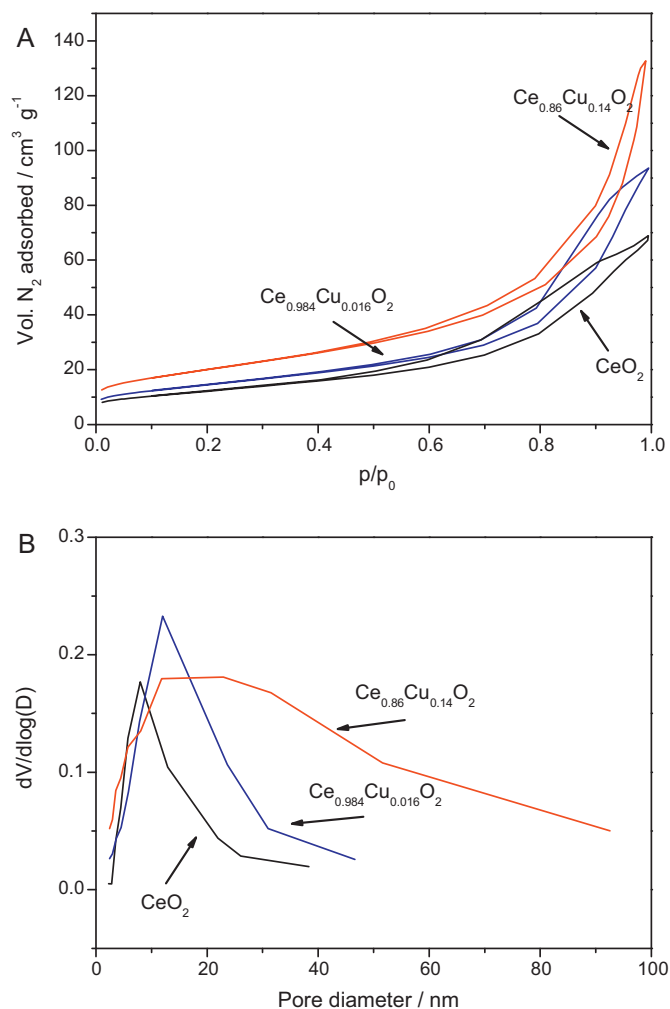

Fig. 3. (A) N_2 adsorption isotherms of some selected mesoporous catalysts. (B) BJH pore size distributions calculated from the desorption branch of the N_2 adsorption isotherms according to the BJH method.

observed that, regardless of the copper content, the XRD patterns of all catalysts are very similar. The diffraction peaks occurred at $2\theta = 29°$, $33.2°$, $47.2°$, $56.3°$, $59.1°$, $69.3°$, $76.8°$ and $78.9°$, which are characteristic of cubic fluorite structured CeO_2 [12]. The X-ray reflections from the mesoporous CeO_2 samples are relatively broad and low in intensity, and this is due to the relatively small size of the nanocrystalline Ce–Cu–O composites. The presence of
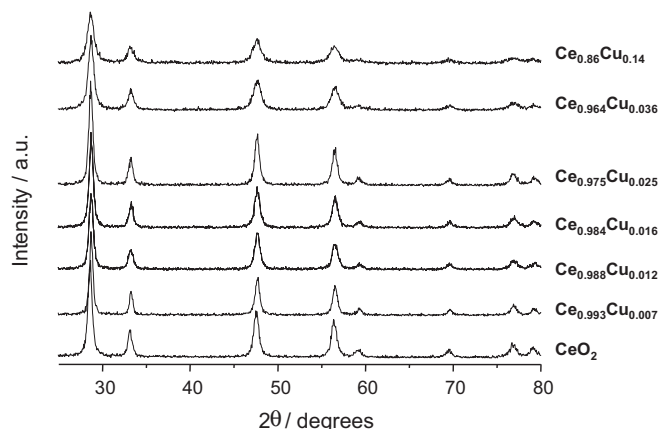

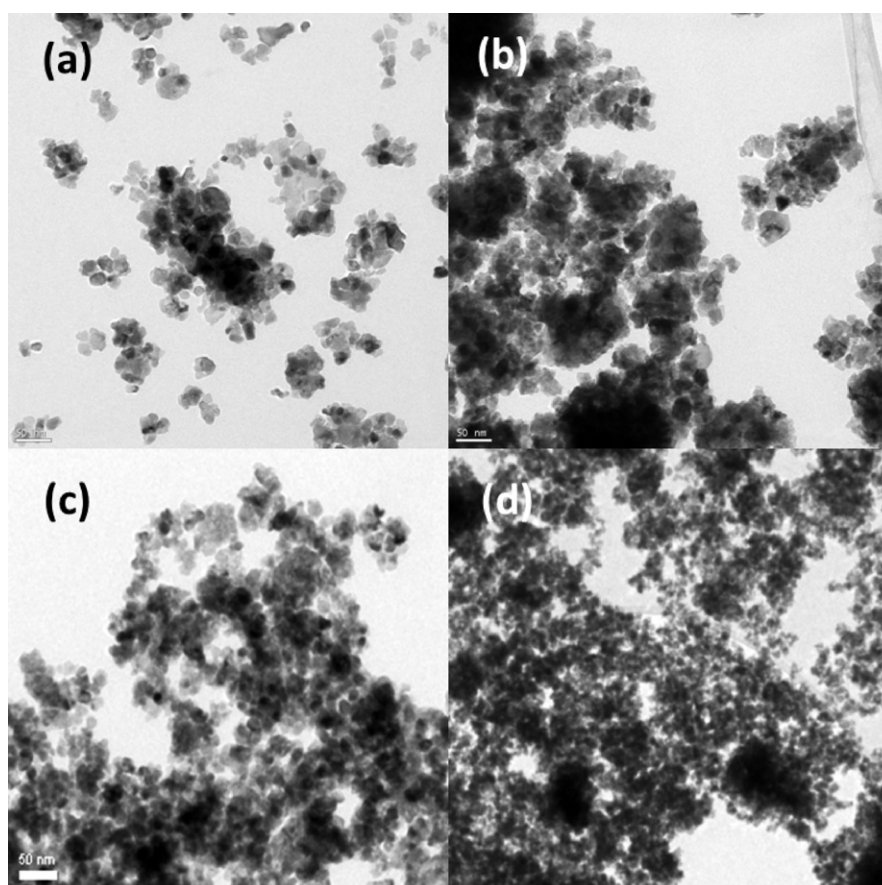**Fig. 4.** XRD patterns of mesoporous ceria and copper ceria catalysts.

Fig. 5. TEM images of copper ceria catalysts with different copper concentrations. Catalysts: (a) CeO_2, (b) $Ce_{0.993}Cu_{0.007}$, (c) $Ce_{0.984}Cu_{0.016}$ and (d) $Ce_{0.86}Cu_{0.14}$. Scale bar is 50 nm.

a marginal diffraction line at $2\theta = 38.7°$, which could be attributed to the (1 1 1) planes of crystalline CuO, cannot be completely ruled out in the catalyst with the highest copper loading. No evidence for the CuO phase was observed for catalysts with lower copper content. Avgouropoulos and co-workers [45], have ascribed the weak or absent diffraction peaks from CuO to well dispersed small CuO species on the surface of CeO_2. Zhu *et al.* also reported that the dispersion capacity of copper species into CeO_2 is limited [46]. When the copper content of the composite is much higher than the dispersion capacity, the size of CeO_2 crystallites decrease and consequently the width of the CeO_2 diffraction peaks become broader. Accordingly in the present work, at low copper content ($\leq 2.5\%$) the ceria crystallite size was very similar to that of pure CeO_2, but at high copper contents a considerable decrease was observed (Table 2). This effect was calculated by application of the

Scherrer equation to XRD data and later confirmed by TEM. Thus, values decreased from approximately 20 nm, for pure CeO_2 and Cu–Ce–O samples with low copper content, to 12 nm for catalysts with higher copper loadings. These data are consistent with the increase of surface area, and this could be a consequence of copper influencing the ceria crystallisation process, which is known to occur when heteroatoms are incorporated into a crystal lattice.

Raman spectra of the CeO_2 catalysts (not shown here) showed similar spectra for all catalysts synthesized, as they presented a single dominant band centred at a frequency of 462 cm^{-1}, which is characteristic of CeO_2 vibrations. Table 2 summarises the full width at half maximum (FWHM) of the main Raman band, at 462 cm^{-1}. Some studies [47] have associated the increase of the FWHM with a decrease of the crystallite size and/or a higher concentration of oxygen vacancies of CeO_2. According to the data from Table 2, a relationship can be established between the mean crystallite size determined by XRD and the Raman band FWHM; as the higher the copper content, the greater the FWHM and the smaller the crystallite size. However, as a consequence of this relationship any influence on the generation of oxygen vacancies by the addition of copper cannot be unequivocally probed by considering the variation of the Raman FWHM, due to the corresponding decrease of crystallite size, which would also result in Raman band broadening. Hence other characterisation techniques are also required to provide information on the catalysts oxygen defects.

TEM and selected area electron diffraction (SAED) analysis of the catalysts were performed on samples deposited over TEM nickel grids. Fig. 5 presents some representative TEM images of copper ceria catalysts with different copper concentrations. Grains with sizes ranging between 7 and 40 nm can be clearly observed from

Table 2
Structural and surface properties of catalysts calculated from XRD and XPS.

Catalyst	FWHM[a] (cm^{-1})	Lattice parameter (Å)	Cryst. size[b] (nm)	O_β/O_α[c]
CeO_2	15.0	5.4150	19.5	0.87
$Ce_{0.993}Cu_{0.007}O_2$	16.7	5.4100	23.4	1.04
$Ce_{0.988}Cu_{0.012}O_2$	16.9	5.3965	18.7	1.51
$Ce_{0.984}Cu_{0.016}O_2$	19.5	5.3995	18.4	1.89
$Ce_{0.975}Cu_{0.025}O_2$	16.5	5.3975	20.3	1.46
$Ce_{0.964}Cu_{0.036}O_2$	27.8	5.3970	12.9	1.78
$Ce_{0.86}Cu_{014}O_2$	41.4	5.3990	11.0	1.00

[a] Full width at half maximum for the Raman band at 462 cm^{-1}.
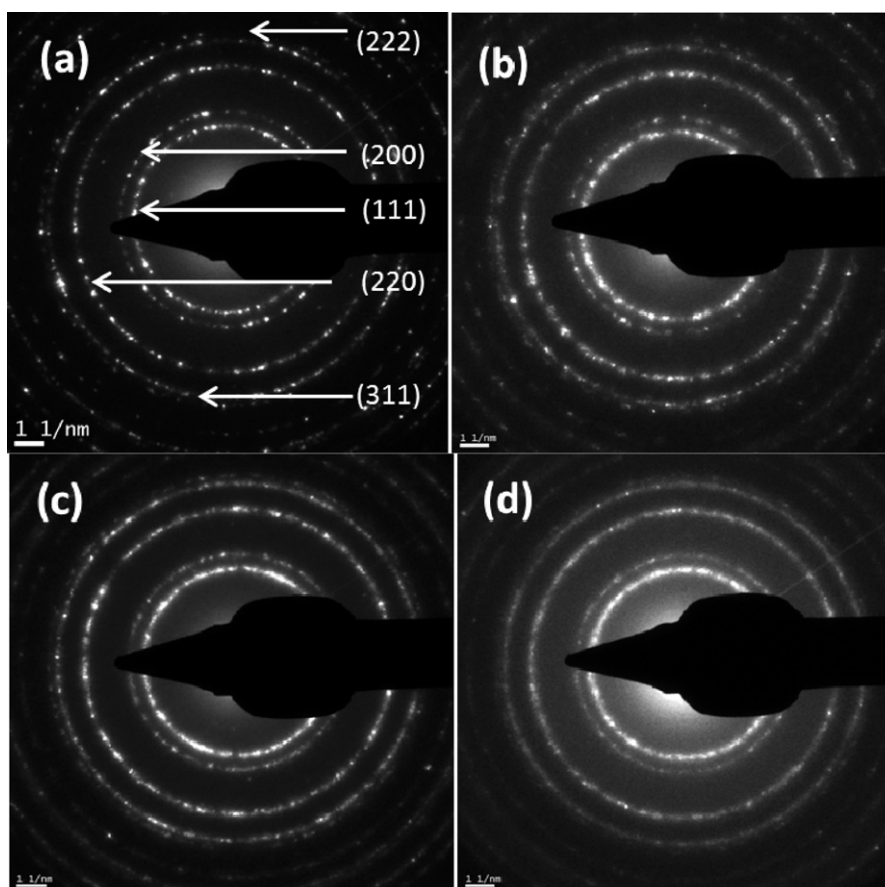[b] Determined from X-ray line broadening.
[c] Determined from XPS.

Fig. 6. SAED patterns recorded from the copper ceria catalysts. Catalysts: (a) CeO_2, (b) $Ce_{0.993}Cu_{0.007}$, (c) $Ce_{0.984}Cu_{0.016}$ and (d) $Ce_{0.86}Cu_{0.14}$.

the micrographs. The addition of copper to CeO_2 seems to increase the level of agglomeration of the grains. The contrasting areas in the micrographs were considered to be due to the varying degrees of particle agglomeration, as local EDX of the contrasting regions indicated that they had similar composition. Additionally, the catalyst with the highest copper loading has the smallest grain size, which is in agreement with the crystallite size determined from XRD data.

Accurate analysis of the unit cell parameters of the catalysts from powder XRD data was difficult, due to the relatively broad diffraction peaks as a consequence of the small crystallite size. Hence SAED was used to establish accurate crystallographic data. SAED analysis (Fig. 6) indicates that the experimental *d*-spacings of pure CeO_2, from the centre to the outer ring are as follows: 3.126, 2.707, 1.914, 1.652 and 1.565 Å, corresponding to the sets of planes (1 1 1), (2 0 0), (2 2 0), (3 1 1) and (2 2 2), respectively. These are indexed to the Face-Centred Cubic (FCC) phase of CeO_2 (JCPDS: 34-394) with space group *Fm3m*. From the inter-planar distance the *a*-lattice parameter of CFC CeO_2 was determined [48]. The analysis showed that the *a*-lattice parameter decreased when increasing the copper content (Table 2). The variation in lattice parameter calculated for copper ceria catalysts is clear evidence of the substitution of Cu^{2+} cations into Ce^{4+} sites in the CeO_2 lattice to form a mixed copper cerium oxide phase.

Careful analysis of the electron diffraction patterns from the copper ceria catalysts revealed that only diffraction rings corresponding to the cubic $Ce_{1-x}Cu_xO_2$ phase were present up to a copper concentration of 3.6%. No diffraction from copper oxide or any other phase was observed in the SAED patterns, indicating that copper was incorporated into the CeO_2 lattice. It is well-known that dopants can change the cell dimensions of the ceria lattice [49,50].

The *a*-lattice parameter of cubic phase $Ce_{1-x}Cu_xO_2$, measured from the SAED patterns, are somewhat lower than those expected for undoped CeO_2, which suggests some incorporation of Cu^{2+} cations into the ceria lattice. The radius of the Cu^{2+} ion is 0.072 nm, which is smaller than that of the Ce^{4+} ion at 0.101 nm. Fig. 7 presents the evolution of *a*-lattice parameter of cubic $Ce_{1-x}Cu_xO_2$ catalysts as a function of copper content. Two distinct regions can be observed, the first shows a rapid essentially linear decrease of the *a*-lattice parameter when the copper content is less than 1.2 at.% and this is in agreement with Vegard's law as copper is substituted into the
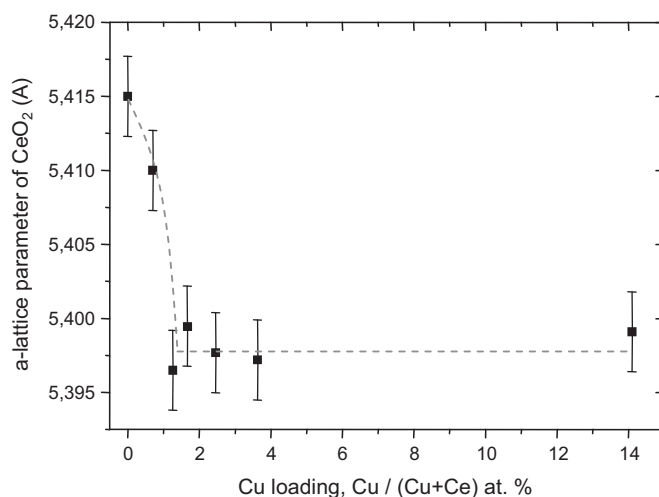

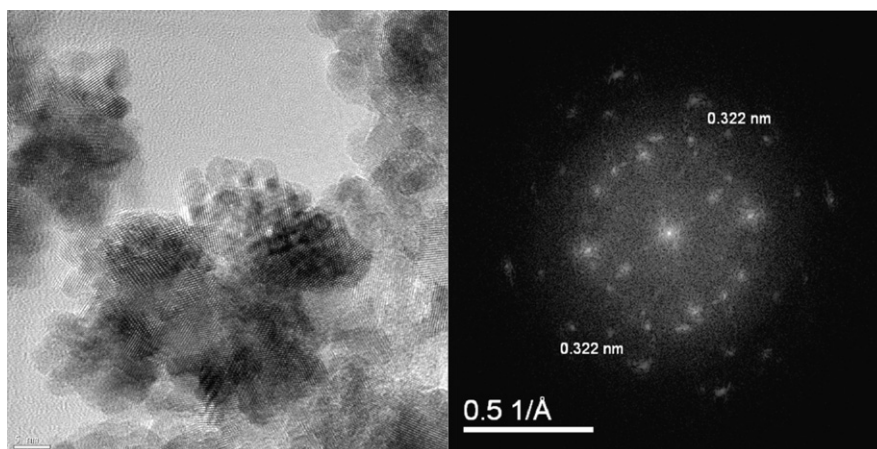**Fig. 7.** Evolution of the *a*-lattice parameter of cubic $Ce_{1-x}Cu_xO_2$ as a function of measured Cu content.

Fig. 8. High resolution TEM and corresponding Fast Fourier Transform (FFT) images, showing the coexistence of both cubic and monoclinic $Ce_{1-x}Cu_xO_2$ structures for the 14% copper catalyst.

ceria lattice. The second region can be observed at higher copper contents and shows a more asymptotic relationship, which could indicate that not all of the copper is incorporated into the ceria lattice.

High resolution TEM and corresponding Fast Fourier Transforms (FFT) analyses of the catalysts with the highest copper content have shown the presence of clear diffraction spots with an interplanar distance of 0.232 nm (Fig. 8). The measured *d*-spacing from FFT is close to that of the (1 1 1) lattice planes of CuO, and is in good agreement with monoclinic CuO with a *Cc* space group. This observation means that there are two different phases present in the higher loading catalyst, i.e. copper cerium mixed oxide and CuO, coexisting. These findings suggest there is a limit of incorporation of copper into the ceria phase and the formation of a discrete CuO phase explains the deviation from Vegard's law observed in the region of higher copper content in Fig. 7. The measured interplanar *d*-spacing from FFT appears slightly larger when compared to pure CuO (JCPDS: 1-080-191) [51], which could be due to some incorporation of the cerium into the monoclinic CuO structure. These results are in agreement with XPS (see below), as a compound of copper oxide was detected for this sample. The remaining spots in the diffraction pattern from the FFT image are assigned to a $Ce_{1-x}Cu_xO_2$ cubic structure.

Compositional analysis of the copper ceria samples was carried out using TEM-EDX measurements. To improve the accuracy of the compositional analysis TEM-EDX spectra from various points of each sample were recorded and the mean value has been taken as representative (Table 1). EDX-mapping (not shown here) revealed that regardless of the catalyst considered, Cu is well dispersed in the ceria matrix and no agglomeration of copper species was observed. Even in the catalyst with the highest copper loading, in which monoclinic CuO was detected, it was observed that small nanoparticles of CuO were well dispersed to surround the ceria particle.

Temperature programmed reduction measurements were carried out to investigate the redox properties of the synthesized catalysts (Fig. 9). TPR profiles for CeO_2 and those copper ceria catalysts with low copper content show a low intensity reduction feature, suggesting that less than 1% of the overall cerium oxide is reduced in the interval of temperatures studied (ambient to 800 °C). In the case of the $Ce_{0.86}Cu_{0.14}O_2$ catalyst, an intense peak centred at 171 °C with a shoulder at 150 °C was observed. These features correspond to the reduction of CuO (CuO → Cu_2O and Cu_2O → Cu [52]). The presence of CuO nanoparticles is in accordance with TEM and XPS data. Fig. 9B shows magnification of the 200–800 °C region. Peaks of low intensity centred between 475 and 550 °C, which can be attributed to surface reduction of ceria capping oxygen, were

observed for all the catalysts [53,54]. This peak was observed at 490 °C for pure CeO_2, meanwhile copper ceria catalysts with lower copper concentrations (2.5 and 3.6%) showed it at slightly lower temperatures of *ca.* 475 °C. These data indicate that incorporation of copper into the ceria lattice increase the mobility of lattice oxygen. However, it must be considered that the intensities of these features are very low and hence the extent of reduction of the catalysts is relatively low. In the case of $Ce_{0.86}Cu_{0.14}O_2$ the peak
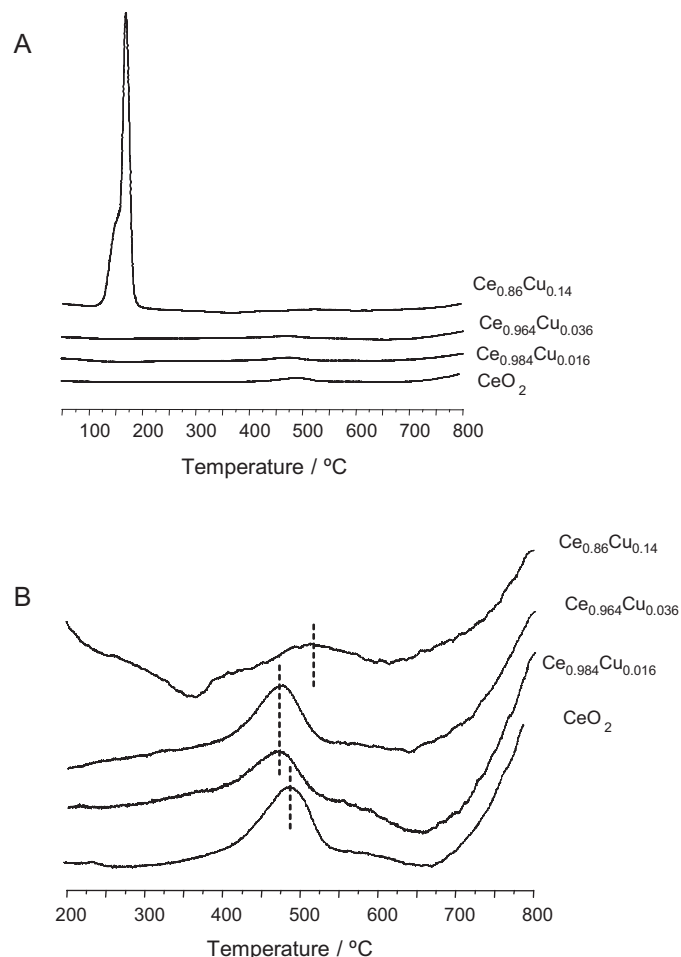

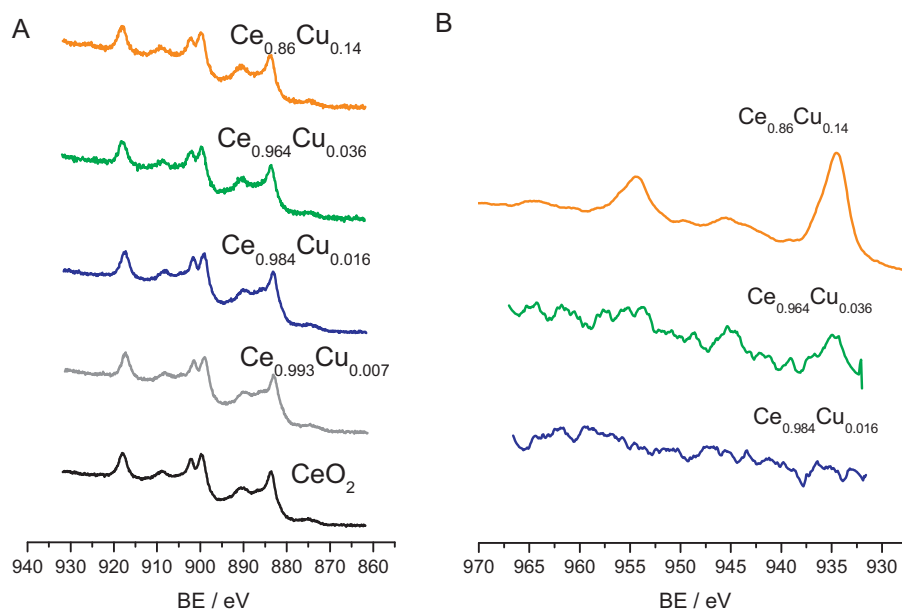**Fig. 9.** TPR profiles for CeO_2 and representative copper doped ceria catalysts.

Fig. 10. Ce3d (A) and Cu2p (B) XPS spectra of CeO_2 and representative copper doped ceria catalysts.

is centred at *ca.* 520 °C. It must be noted that our experiments have been conducted up to 800 °C, and therefore the reduction of the bulk CeO_2 is not fully recorded. The onset at *ca.* 675 °C observed for all the catalysts correspond to the start of the reduction of bulk ceria [55].

XPS survey spectra of Cu–Ce–O catalysts with various copper contents have been conducted in order to probe the surface characteristics of the catalysts. Fig. 10 shows the XPS spectra of Ce3d and Cu2p. In the case of cerium species, (see Fig. 10A), no appreciable major differences between catalysts were observed. Two principal peaks of $Ce3d_{5/2}$ and $Ce3d_{3/2}$, and four satellite peaks, resulting from ionization attributed to Ce(IV), can be observed. The five peaks appeared at 883.7, 890.5, 899.6, 902.4, 909.0 and 918.0 eV, respectively and the peak binding energies were the same regardless of the catalysts studied. Thus, it can be concluded that the main valence of surface cerium was Ce^{4+} [56], albeit the existence of a low percentage of Ce^{3+} cannot be ruled out since marginal shoulders at 886.0 and 904.2 eV were observed [57].

In the case of photoemission from copper, the Cu2p signal was only clearly observed in the case of the catalyst with the highest, 14%, copper content, (see Fig. 10B), likely to be related to the copper nanoparticles detected by TEM. This signal consisted of two main peaks of $Cu2p_{3/2}$ centred at 934.2 eV and $Cu2p_{1/2}$ centred at 954.2 eV, with shake-up peaks centred at 945 eV. A high binding energy for the $Cu2p_{3/2}$ and the shake-up peaks are most likely attributed to Cu^{2+} species in copper oxide nanoparticles, but the relative intensity of this satellite with respect to the main peak is lower than 0.55. This fact suggests the presence of some reduced copper species (Cu^+). Accordingly, the corresponding kinetic energy spectra of Cu L3VV electron consisted of a main peak at 916.8 eV. Jernigan and Somorjai [58] found kinetic energies of 918.5 eV for Cu_0, 916.5 eV for Cu_2O, and 917.6 eV for CuO. Thus, the Cu 2p XP spectra can be attributed to the simultaneous presence of Cu^+ and Cu^{2+}. The presence of reduced states (either Cu^+ or Ce^{3+}) in initial calcined catalysts has already been reported by different authors [45,59]. Finally, the spectra of copper ceria catalysts with lower Cu-loading showed very low intensity Cu2p peaks and this is consistent with the majority of copper being dispersed throughout the ceria lattice, rather than surface dispersed copper nanoparticles.

XPS studies concentrating on the oxygen species were also conducted. The XPS spectra of the O1s region (Fig. 11) clearly show

two surface oxygen species. According to Hardacre *et al.* [60], the binding energy of 529–530 eV is characteristic of the lattice oxygen (O^{2-}) and is denoted as O_α, and the binding energy in the region of 531–533 eV may be assigned to defect oxide or to low coordination surface oxygen ions (denoted as O_β). In addition, the presence of surface hydroxyl or carbonate species can also contribute to this peak. Hence, DRIFTS analyses of the mesoporous samples were carried out in order to assess any possible contribution to this peak of oxygen species either in surface hydroxyl or carbonates. DRIFTS spectra of selected catalysts collected after oxidative activation with synthetic air at 400 °C for 30 min are shown in Fig. 12. It can be observed that these spectra presented quite similar features for all catalysts, with only some marginal differences in each one of the three characteristic vibrational regions: 4000–3200 cm^{-1} (OH vibrations), 3200–2700 cm^{-1} (CH vibrations) and 2000–800 cm^{-1} (CO/CC vibrations). Thus, the spectra of all samples presented three
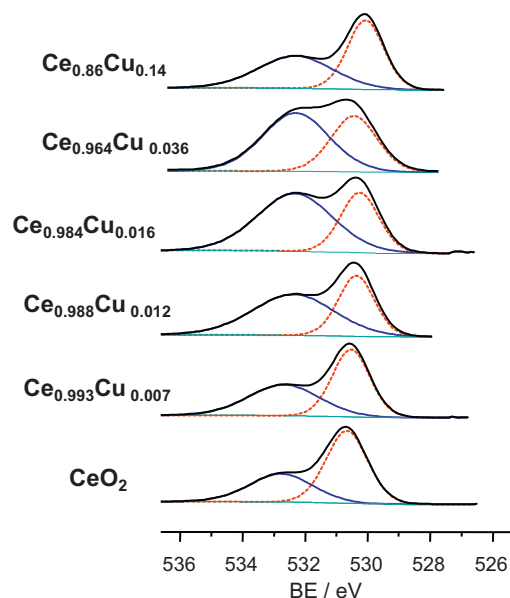

Fig. 11. O1s XPS spectra of CeO_2 and representative copper doped ceria catalysts.
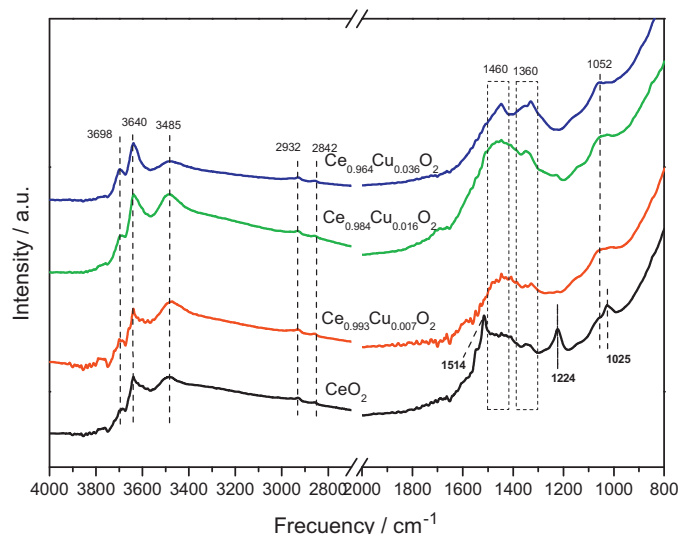
Fig. 12. DRIFTS spectra of selected catalysts after treatment 30 min at 400 °C in synthetic air.

Fig. 13. Variation of the O_β/O_α ratio determined by XPS as a function of copper loading.

bands in the OH vibrational region. The band at 3698 cm^{-1} was assigned to mono-coordinated OH (type I) groups; the band at 3640 cm^{-1} was assigned to bridging OH (type II) groups and a broad band centred at 3485 cm^{-1} was assigned to hydroxyl groups of a ceria oxyhydroxide phase [61]. No major differences were observed for both the frequency and the relative intensities of these peaks, indicating that concentrations of surface hydroxyl species were all broadly similar. In addition, although the assignment of stretching vibration modes of the O—C—O group of carbonate species is complicated, and their detailed analysis is beyond the scope of this manuscript, it can be observed that all copper doped ceria catalysts presented similar broad bands around 1460 and 1330 cm^{-1} and a less pronounced band at 1052 cm^{-1}, which were characteristic of bulk-type polydentate carbonates [61–63]. Only the pure CeO$_2$ catalyst presented other low intensity peaks at 1514, 1224 and 1025 cm^{-1} that could be assigned to carboxylate, bridged carbonate and bidentate carbonate, respectively [64]. Therefore, it can be concluded that all the copper doped ceria catalysts presented similar amounts of both hydroxyl and carbonate surface groups, which should exert similar contribution to the signal of the O_β XPS peak regardless of the copper content and therefore variations in the O_β peak areas can be linked to the presence of different amounts of oxygen defects on the catalyst surface. The peak area ratios for both surface oxygen species are shown as a function of the copper loading in Fig. 13. It can be observed that with the increase of copper content from 0 to 1.6 at.%, the relative amount of O_β species increases as O_β/O_α increases from 0.87 to 1.89. For higher copper contents the O_β/O_α ratio then begins to decrease to 1.00 at the highest copper content. This suggests that copper contents higher than those that can be accommodated into the ceria lattice lead to a lower concentration of defects on the catalyst surface.

3.3. Comments on the relationship between characterisation and catalyst performance

Copper doped ceria catalysts clearly have high activity for the total oxidation of naphthalene. Specifically the Ce$_{0.984}$Cu$_{0.016}$O$_2$ was the most active. Catalytic activity of 90% conversion to carbon dioxide, using a very high space velocity of 75,000 h^{-1}, was achieved at only 220 °C, which is among the best catalysts reported (Table 3). It is significant that the addition of a low amount of copper to the ceria has led to a large increase of the yield to carbon dioxide, which reached a maximum at a copper loading of 1.6%.
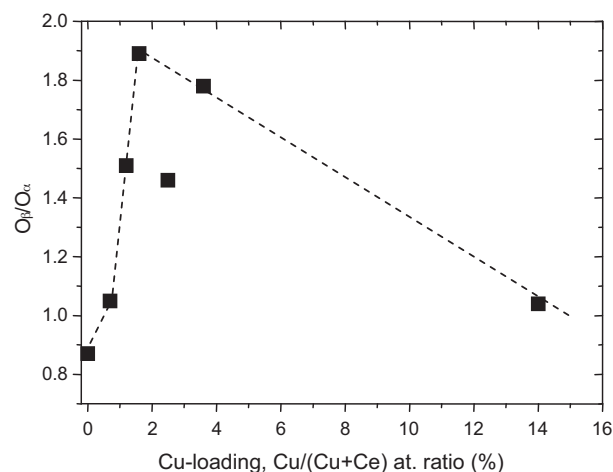
The addition of copper to CeO$_2$ resulted in a slight increase of the catalyst surface area, from 43 up to 50 m^2 g^{-1}, for copper contents up to 2.5%. A further increase of the copper loading led to a substantial increase of surface area up to 70 m^2 g^{-1}. However, the enhanced catalytic activity is not directly related to the increased surface area, as the activity normalized for surface area is still greatest for the 1.6% copper ceria catalyst (Table 1).

XPS studies have shown that the addition of low amounts of copper increased the proportion of a specific O-species (denoted as O_β), which corresponds to oxide defects or to low coordination surface oxygen ions, since DRIFTS shows that concentrations of surface hydroxyl and carbonate groups remain constant. However, higher copper loadings led to a decrease of these species. The trend of surface defect concentration with copper content is the same as the trend shown by the activity of the range of catalysts for naphthalene oxidation (Fig. 14a). Therefore, the presence of the surface O_β species seems to be directly related to the catalytic activity. It is thought that the surface oxygen defects are very reactive, and can easily activate the reactants, in this case naphthalene and oxygen, increasing the activity. The synthesis of the catalysts has incorporated copper into the CeO$_2$ lattice

Table 3
Comparison of naphthalene total oxidation activity on the basis of the temperature required for specified naphthalene conversion of 10, 50 and 90% to CO$_2$, denoted as T_{10}, T_{50} and T_{90}, respectively.

Catalyst	T_{10} (°C)	T_{50} (°C)	T_{90} (°C)	GHSV (h^{-1})	Reference
Ce$_{0.984}$Cu$_{0.016}$O$_2$[a]	165	200	220	75,000	This work
Ce-KIT6-80[a]	210	235	275	75,000	[16]
Ce-KIT6-80[a]	165	215		240	20,000
1%Pt/Al$_2$O$_3$[b]	240		280	20,000	[5]
1%Pd/Al$_2$O$_3$[b]	253		285	20,000	
0.12%Pt/Al$_2$O$_3$[c]	194	204	310	20,000	[69]
Cu/Mn/Al$_2$O$_3$[c]	180	207		20,000	
CeO$_2$ (urea)[d]	110	160	190	25,000	[54]
CeO$_2$ (urea)[e]	160	190	210	60,000	[70]
Mn$_2$O$_3$[e]	185	230	250	60,000	
CeO$_2$ (carbonate)[e]	260	300	320	60,000	
Co$_3$O$_4$[e]	215	245	270	60,000	
Ce$_{0.75}$Zr$_{0.25}$O$_2$[f]	225	250	280	240,000	[71]

[a] 450 ppmv naphthalene, 20 vol.% O$_2$; conversion in terms of CO$_2$ yield.
[b] 100 ppmv naphthalene, 10 vol.% O$_2$; conversion in terms of CO$_2$ yield.
[c] 50 ppmv naphthalene, 200 ppmv CH$_4$, 2550 ppmv CO, 12 vol.% CO$_2$, 10 vol.% O$_2$, 0–20 vol.% H$_2$O; conversion in terms of C$_8$H$_{10}$ destruction.
[d] 100 ppmv naphthalene, 20 vol.% O$_2$; conversion in terms of CO$_2$ yield.
[e] 100 ppmv naphthalene, 20 vol.% O$_2$; conversion in terms of CO$_2$ yield.
[f] 200 ppmv naphthalene, 10% O$_2$ and balance He (200 ml min^{-1}), 50 mg of catalyst; conversion in terms of C$_8$H$_{10}$ destruction.
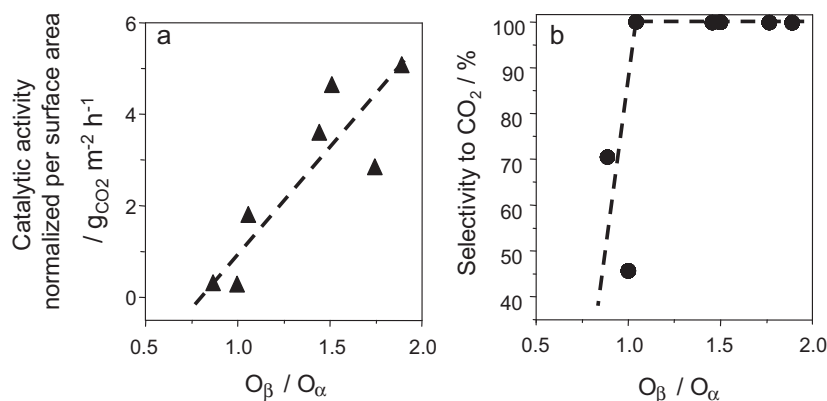
Fig. 14. Relationship between the nature of the surface O-species and (a) the specific catalytic activity or (b) the selectivity to carbon dioxide. *Notes*: Specific activity is the catalytic activity normalized per unit surface area at 200 °C expressed as g_{CO_2} m^{-2} h^{-1}. O_β/O_α is the ratio between the concentration of these two O-species detected by XPS. Selectivity to CO_2 at 20% naphthalene conversion.

as confirmed by the variation of the lattice parameter (Table 2), and this produces a higher density of oxygen defect sites. The introduction of a range of heteroatoms into the lattice of metal oxides has already been reported to distort the unit cell of the metal oxide generating more oxygen defects [65]. For catalysts with higher copper content the mesoporous CeO_2 structure is not capable of incorporating more copper into the cubic fluorite lattice and hence copper nanoparticles are formed. Consequently catalysts with higher copper content have a lower concentration of surface defects and this is reflected in the lower catalytic activity.

Moreover, for naphthalene oxidation the addition of copper has also induced an increase in the selectivity to CO_2 (Fig. 14b). From data in Table 1 it can be observed that, at 20% isoconversion, pure CeO_2 presents a selectivity to carbon dioxide of 70%, meanwhile only CO_2 was detected for copper ceria catalysts with a copper content <3.6%. A further increase of the copper content led to a decrease in the selectivity to CO_2 (46%). The decrease can be related to the lower concentration of oxygen defects and also to the lower selectivity towards CO_2 exhibited by CuO, which has been identified on the catalyst. It has been previously reported [13] that the presence of a high concentration of O-defects facilitates the deep oxidation of naphthalene increasing the selectivity towards CO_2. The oxygen vacancies are not only likely to influence naphthalene oxidation, but they are also likely to be involved in the surface oxidation of any partially oxidised naphthalene intermediates, and hence increase CO_2 selectivity.

The oxidation of naphthalene has been reported to take place via a Mars–van Krevelen mechanism for a cerium oxide catalyst [34], in which oxygen from the lattice is used for the oxidation of the hydrocarbon. This same type of mechanism can also operate for these copper doped ceria catalysts, since naphthalene oxidation products could be detected on the catalyst surface by in situ DRIFTS analysis under a non-oxidising atmosphere. DRIFTS experiments were conducted at 250 °C by exposing the catalyst to naphthalene in a flow of N_2 in order to study the adsorption of naphthalene over the catalyst surface, and the first oxidative steps that involve the surface and lattice oxygen species. Spectra of representative catalysts after 90 min of reaction are shown in Fig. 15. Copper doped ceria catalysts presented remarkable features in all three regions of their DRIFTS spectra. In the OH stretching region, peaks at 3698, 3640 and 3485 cm^{-1} had mostly disappeared (compared with Fig. 12) and two negative bands assigned to singly and doubly coordinated hydroxyls centred at 3698 and 3623 cm^{-1}, respectively, were observed. These negative peaks indicate that the corresponding surface hydroxyls were consumed by either adsorption or reaction of naphthalene. Accordingly, two broad bands around 1540 and 1405 cm^{-1} appeared in

the CC/CO stretching region, which can be assigned to surface naphthoate species [66] after naphthalene chemisorption at the hydroxyl groups. These naphthoate species could represent one of the modes of adsorption of naphthalene on the catalyst surface and at the same time, the first step towards its oxidation. Naphthoate could then be oxidised in a second step leading to the formation of phthalate compounds, since the characteristic vibrations of phthalates have been detected at 1150 and 1082 cm^{-1} [67,68]. Other products of naphthalene further oxidation are formate species characterised by two sharp peaks present at 1371 and 1356 cm^{-1}, assigned to bidentate and bridged formates, respectively [64]. It is worth highlighting that the $Ce_{0.964}Cu_{0.036}O_2$ catalyst showed very sharp and well pronounced bands for naphthoate vibrations (1540 and 1405 cm^{-1}) when compared to the $Ce_{0.984}Cu_{0.016}O_2$ catalyst, but both showed the same consumption of OH surface groups. Hence, it seems that although a Mars–van Krevelen type mechanism takes place for all the copper doped ceria catalysts, those catalysts doped with higher amounts of copper showed similar surface adsorption but lower oxidation rate towards phthalate and formate species (i.e. lower activity). This feature is in agreement with the catalytic activity presented in Fig. 1 and could be related to the higher amount of oxygen surface defects shown for the $Ce_{0.984}Cu_{0.016}O_2$ catalyst. Accordingly, the $Ce_{0.993}Cu_{0.007}O_2$ catalyst, which presents intermediate catalytic activity between
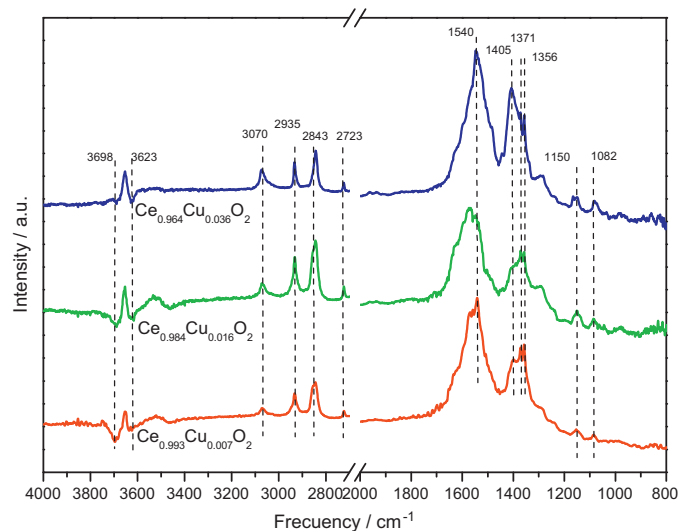

Fig. 15. DRIFTS spectra of selected catalysts after treatment for 90 min at 250 °C in naphthalene/N_2.

$Ce_{0.964}Cu_{0.036}O_2$ and $Ce_{0.984}Cu_{0.016}O_2$, also showed CC/CO stretching peaks that were intermediate, with a clear oxidative capacity but it was not as great as the $Ce_{0.984}Cu_{0.016}O_2$ catalyst. Finally, four well resolved peaks in the CH region can be assigned to naphthalene adsorption ($3070\,cm^{-1}$) and subsequent formate products from naphthalene oxidation (2935, 2843 and $2723\,cm^{-1}$) [64], consistent with the presence of all the species discussed above. Again, it is observed that a less active catalyst ($Ce_{0.964}Cu_{0.036}O_2$) shows more adsorption features (peak at $3070\,cm^{-1}$) and less oxidation products (peaks at 2935, 2843 and $2723\,cm^{-1}$) than the most active one ($Ce_{0.984}Cu_{0.016}O_2$). These facts, together with the lack of agreement between TPR and catalytic data, indicates that activity is not simply related directly to the ease of availability of lattice oxygen and that adsorbed oxygen at the surface defects plays a important role for PAH oxidation.

4. Conclusions

Mesoporous ceria is an active catalyst for the total oxidation of naphthalene. The addition of low amounts of copper to the ceria significantly increases the catalytic activity and the selectivity towards CO_2. Naphthalene total oxidation activity increased as the copper content was increased up to 3.6 at.%, but decreased when it was increased further to 14%. The increase of activity was due to the incorporation of copper into the ceria lattice, which led to an increased concentration of surface defects, as observed by XPS and DRIFTS studies. The decrease of activity at higher copper content was due to the decrease of the concentration of surface oxygen defects and to the presence of catalytically less active CuO dispersed on the $Ce_{1-x}Cu_xO_2$ catalyst surface.

References

[1] G. Moretti, C. Dossi, A. Fusi, S. Recchia, R. Psaro, Applied Catalysis B: Environmental 20 (1999) 67.
[2] M. Karthik, L-Yi Lin, H. Bai, Microporous and Mesoporous Materials 117 (2009) 153.
[3] W.B. Li, J.X. Wang, H. Gong, Catalysis Today 148 (2009) 81.
[4] N.E. Ntainjua, T. Garcia, S.H. Taylor, Catalysis Letters 110 (1–2) (2006) 125.
[5] X.W. Zhang, S.C. Shen, L.E. Yu, S. Kawi, K. Hidajat, K.Y. Simon, Applied Catalysis A: General 250 (2) (2003) 341.
[6] Z. Yun-feng, H. Chi, X. Qi, C. Xing, C. Jin-sheng, Journal of Fuel Chemistry and Technology 39 (7) (2011) 543.
[7] M. Hosseini, S. Siffert, R. Cousin, A. Aboukais, Z. Hadj-Sadok, B.-L. Su, Comptes Rendus Chimie 12 (2009) 654.
[8] D.A. Aguilera, A. Perez, R. Molina, S. Moreno, Applied Catalysis B: Environmental 104 (2011) 144.
[9] M.S. Vasilyeva, V.S. Rudnev, F. Wiedenmann, S. Wybornov, T.P. Yarovaya, X. Jiang, Applied Surface Science 258 (2011) 719.
[10] J. Deng, L. Zhang, H. Dai, C.-T. Au, Applied Catalysis A: General 352 (2009) 43.
[11] A.K. Sinha, K. Suzuki, Applied Catalysis B: Environmental 70 (2007) 417.
[12] B. Solsona, E. Aylon, R. Murillo, A.M. Mastral, A. Monzonis, S. Agouram, T.E. Davies, S.H. Taylor, T. Garcia, Journal of Hazardous Materials 187 (2011) 544.
[13] A. Aranda, J.M. López, R. Murillo, A.M. Mastral, A. Dejoz, I. Vázquez, B. Solsona, S.H. Taylor, T. García, Journal of Hazardous Materials 171 (2009) 393.
[14] F. Ying, S. Wang, C.-T. Au, S.-Y. Lai, Microporous and Mesoporous Materials 142 (2011) 308.
[15] A. Aranda, B. Puértolas, B. Solsona, S. Agouram, R. Murillo, A.M. Mastral, S.H. Taylor, T. Garcia, Catalysis Letters 134 (2010) 110.
[16] B. Puertolas, B. Solsona, S. Agouram, R. Murillo, A.M. Mastral, A. Aranda, S.H. Taylor, T. García, Applied Catalysis B: Environmental 93 (2010) 395.
[17] L.C. Marr, T.W. Kirchstetter, R.A. Harley, A.H. Miguel, S.V. Hering, S.K. Hammond, Atmospheric Environment 33 (18) (1999) 2955.
[18] A.M. Mastral, T. García, R. Murillo, M.S. Callén, J.M. López, M.V. Navarro, Industrial and Engineering Chemistry Research 42 (2003) 155.
[19] P.J. Kirton, P.T. Crisp, Fuel 69 (5) (1990) 633–638.
[20] P. Li, Xi Li, F. Stagnitti, H. Zhang, X. Lin, S. Zang, J. Zhuo, X. Xiong, Journal of Hazardous Materials 162 (2009) 463.
[21] Environment European Agency, http://prtr.ec.europa.eu.
[22] International Agency for Research on Cancer (IARC), Chemical Environmental and Experimental Data, Polynuclear Aromatic Compounds, Part 1, Lyon, France, 1983.
[23] M.E. Burczynski, T.M. Penning, Cancer Research 60 (2000) 908.
[24] Evaluation and Estimation of Potential Carcinogenic Risks of PAH: Carcinogen Assessment; Office of Health and Environmental Assessment, Office of Research and Development, U.S., EPA, U.S. Government Printing Office, Washington, DC, 1985.
[25] UNO 1998 Protocol to the 1979 Convention on Long-Range Transboundary Air Pollution on Persistent Organic Pollutants.
[26] R.W. Coutant, L. Brown, J.C. Chaung, R.M. Riggin, R.G. Lewis, Atmospheric Environment 22 (1988) 403.
[27] J.J. Cudahy, R.W. Helsel, Waste Management 20 (5–6) (2000) 339.
[28] S. Santos, K. Jones, R. Abdul, J. Boswell, J. Pacac, Biochemical Engineering Journal 37 (2007) 261.
[29] R.E. Hester, R.M. Harrison, Volatile Organic Compounds in the Atmosphere, The RSC Cambridge, 1995.
[30] B.J. Park, G.S. Hwang, S.J. Haam, C.H. Lee, I.S. Ahn, K.J. Lee, Journal of Hazardous Materials 153 (2008) 735.
[31] M.S. Callen, M.T. De La Cruz, S. Marinov, A.M. Mastral, R. Murillo, M. Stefanova, Fuel Processing Technology 88 (2007) 273.
[32] S. Scire, S. Minico, C. Crisafulli, C. Satriano, A. Pistone, Applied Catalysis B: Environmental 40 (2003) 43.
[33] A.K. Neyestanaki, L.E. Lindfors, Fuel 77 (1998) 1727.
[34] E.N. Ntainjua, S.H. Taylor, Topics in Catalysis 52 (2009) 528.
[35] P.H. McMurry, Atmospheric Environment 34 (2000) 1959.
[36] Y.P. Sun, H.P. Wang, C.Y. Peng, T.L. Hsiung, Y.M. Sun, Y.-. Huang, Radiation Physics and Chemistry 75 (2006) 1926.
[37] J. Bao, Z. Liu, Y. Zhang, N. Tsubaki, Catalysis Communications 9 (2008) 913.
[38] D. Fang, W. Ren, Z. Liu, X. Xu, L. Xu, H. Lu, W. Liao, H. Zhang, Journal of Natural Gas Chemistry 18 (2009) 179.
[39] E. Moretti, L. Storaro, A. Talon, M. Lenarda, Catalysis Communications 10 (2009) 522.
[40] G. Li, D. Qu, Z. Wang, C. Su, Y. Tong, L. Arurault, Chemical Communications 48 (2009) 7557.
[41] H. Mai, D. Zhang, L. Shi, T. Yan, H. Li, Applied Surface Science 257 (2011) 7551.
[42] C. Hu, Q. Zhu, Z. Jiang, Y. Zhang, Y. Wang, Microporous and Mesoporous Materials 113 (2008) 427.
[43] A. Aranda, E. Aylón, B. Solsona, R. Murillo, A.M. Mastral, D.R. Sellick, S. Agouram, T. García, S.H. Taylor, Chemical Communications 48 (2012) 4704–4706.
[44] J. Roggenbuck, H. Schäfer, T. Tsoncheva, C. Michev, J. Hass, M. Tiemann, Microporous and Mesoporous Materials 101 (2007) 335.
[45] G. Avgouropoulos, T. Ioannides, H. Matralis, Applied Catalysis B: Environmental 56 (2005) 87.
[46] J. Zhu, L. Zhang, Y. Deng, B. Liu, L. Dong, F. Gao, K. Sun, L. Dong, Y. Chen, Applied Catalysis B: Environmental 96 (2010) 449.
[47] E.N. Ntainjua, T. Garcia, B. Solsona, S.H. Taylor, Applied Catalysis B: Environmental 76 (2007) 248.
[48] B.D. Cullity, S.R. Stock, Elements of X-rays Diffraction, third ed., Prentice Hall, NJ, USA, 2001, p. 619 (Appendix A).
[49] X. Wang, J.C. Hanson, G. Liu, J.A. Rodríguez, A. Iglesias-Juez, M.J. Fernández-García, Chemical Physics 121 (2004) 5434.
[50] X. Wang, J.C. Hanson, J.A. Rodriguez, C. Belver, M.J. Fernandez-García, Chemical Physics 122 (2005) 154711.
[51] X. Wang, J.A. Rodriguez, J.C. Hanson, D. Gamarra, A. Martínez-Arias, M. Fernandez-García, Journal of Physical Chemistry B 109 (2005) 19595.
[52] G. Fierro, M. Lo Jacono, M. Inversi, P. Porta, F. Cioci, R. Lavecchia, Applied Catalysis A: General 137 (1996) 327.
[53] H.C. Yao, Y. Yu, Journal of Catalysis 86 (1984) 254.
[54] T. Garcia, B. Solsona, S.H. Taylor, Catalysis Letters 105 (2005) 183.
[55] D. Andreeva, R. Nedyalkova, L. Ilieva, M.V. Abrashev, Applied Catalysis B: Environmental 52 (2004) 157.
[56] H.B. Zou, X.F. Dong, W.M. Lin, Applied Surface Science 253 (2006) 2893–2898.
[57] Z. Shanghong, B. Xue, W. Xiaoyan, L. Yuan, Journal of Rare Earths 24 (2006) 177–181.
[58] G. Jernigan, G.A. Somorjai, Journal of Catalysis 147 (1994) 567.
[59] A. Martínez-Arias, A.B. Hungría, G. Munuera, D. Gamarra, Applied Catalysis B 65 (2006) 207–216.
[60] C. Hardacre, G.W. Roe, R.M. Lambert, Surface Science 326 (1995) 1.
[61] F.C. Meunier, D. Tibiletti, A. Goguet, D. Reid, R. Burch, Applied Catalysis A: General 289 (2005) 104.
[62] C. Binet, M. Daturi, J.-C. Lavalley, Catalysis Today 50 (1999) 207.
[63] F. Romero-Sarria, L.M.T. Martínez, M.A. Centeno, J.A. Odriozola, Journal of Physical Chemistry C 111 (2007) 14469.

[64] O. Pozdnyakova, D. Teschner, A. Wootsch, J. Kröhnert, B. Steinhauer, H. Sauer, L. Toth, F.C. Jentoft, A. Knop-Gericke, Z. Paál, R. Schlögl, Journal of Catalysis 237 (2006) 1.

[65] J.L. Gautier, E. Rios, M. Gracia, J.F. Marco, J.R. Gancedo, Thin Solid Films 311 (1997) 51.

[66] K. Hanna, C. Carteret, Chemosphere 70 (2007) 178.

[67] J. Lichtenberger, M.D. Amiridis, Catalysis Today 98 (2004) 447.

[68] K.D. Dobson, A.J. McQuillan, Spectrochimica Acta, Part A 56 (2000) 557.

[69] J. Carnö, M. Berg, S. Järås, Fuel 75 (1996) 959.

[70] T. García, B. Solsona, S.H. Taylor, Applied Catalysis B: Environmental 66 (2006) 92.

[71] A. Bampenrat, V. Meeyoo, B. Kitiyanan, P. Rangsunvigit, T. Rirksomboon, Catalysis Communications 9 (2008) 2349.